Vibration Compensation of an Extendable Variable-Stiffness Boom-Lift-Mounted Robot

Yi Zhou and Molong Duan, *Member, IEEE*

***Abstract*—Boom lifts are commonly utilized in various industries to provide safe and efficient access to elevated work areas. Recently, a boom-lift-mounted robot (BLMR) concept has been proposed, combining a boom lift and an industrial robot to facilitate enhanced levels of construction automation. However, boom lifts typically contain extendable large-scale, variable-stiffness structures, subject to complex nonlinear static deformation, and dynamic motion/gust-induced vibrations. These issues hinder the BLMR's precise and safe operation. To address these issues, this article proposed a static deformation compensation scheme and a vibration alleviation method based on the inertial measurement unit (IMU). The deformation exploits the measurement from a laser tracker, while the vibration compensation method synergistically exploits the extended Kalman filter of the IMU measurements at the tip and the robot motion's dynamic contribution to vibration under a real-time feedback framework. A telescope-type BLMR prototype is built to verify the proposed method. The proposed method is compared with a time-varying input shaper concerning the extension-dependent natural frequencies and damping ratios. Enhanced accuracy of the BLMR operation has been experimentally illustrated.**

***Index Terms*—Boom-lift-mounted robot, construction robot, extension-dependent vibration, vibration compensation.**

I. Introduction

CONSTRUCTION robots are increasingly adopted in the modern construction industry due to rapid urbanization, workforce shortages, safety concerns, and potential applications in extraterrestrial habitats [1]. Among various construction tasks [2] (site preparation, substructure, and superstructure), construction surface work is a labor-intensive and time-consuming process, characterized by the frequent need for maintenance [3].

Manuscript received 10 January 2024; revised 27 March 2024; accepted 10 May 2024. Date of publication 5 June 2024; date of current version 16 August 2024. Recommended by Technical Editor T. Shimono and Senior Editor Q. Zou. This work was supported in part by HKUST Bridge Gap Fund under Grant BGF-2022-026 and in part by Frontier Technology Research for Joint Institutes with Industry Scheme under Grant OKT24EG07. *(Corresponding author: Molong Duan.)*

Yi Zhou is with the The Hong Kong University of Science and Technology, Hong Kong.

Molong Duan is with the The Hong Kong University of Science and Technology, Hong Kong, and also with the HKUST Shenzhen-Hong Kong Collaborative Innovation Research Institute, Futian 518060, China.

Color versions of one or more figures in this article are available at https://doi.org/10.1109/TMECH.2024.3402054.

Digital Object Identifier 10.1109/TMECH.2024.3402054

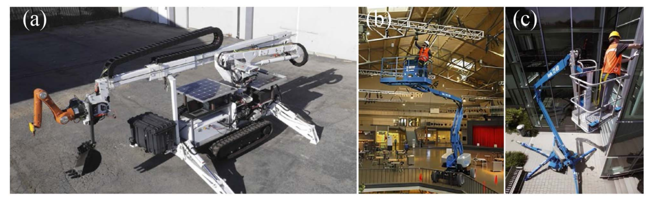

Fig. 1. (a) BLMR prototype [7] and boom-lift enabled construction surface, (b) inspection, and (c) repair [8].

Automating construction surface work poses significant challenges due to dynamic environmental disturbances, interaction forces, and diverse external wall layouts [4]. To address these challenges, representative construction surface work automation platforms, including quadcopters, exterior wall robots, and climbing robots, have been proposed [1], [6], [7]. Exterior wall robots mostly add robotic manipulators to a hanging basket. They are a low-cost automation solution while limited to a flat wall without obstacles (e.g., a balcony) [5]. The climbing robot is designed for nondestructive evaluation tasks like inspection with a low payload [6]. Quadcopters can quickly fly over unstructured terrain but have limited payload and short endurance [1]. To address these abovementioned challenges, recent investigations [7] proposed combining the industrial robot with a boom lift, which is the universal construction surface work platform, as shown in Fig. 1(a).

Boom lifts, as the most commonly exploited high-altitude platform, can be efficiently deployed to accommodate complex construction surface environments and tasks [8], [10]. Currently, they are operated by construction workers to reach designated heights for maintenance, cleaning, repairing, and inspection work, as shown in Fig. 1(b) and (c). Boom lifts, based on the structure extension types, are classified as scissor lifts, vertical mast lifts, telescopic lifts, articulating lifts, and their hybrid combinations (as shown in Fig. 2). Among these types, the scissor lift and vertical mast lift only provide vertical motion and are relatively easy to control. These two types are typically exploited for low-altitude elevation. Telescopic boom lifts and their variants provide the potential to cover a large range of operating altitudes. Also, it is the most representative platform for potential boom-lift-mounted-robot (BLMR) automation, but telescopic boom suffers significantly from vibrations due to the extendable long beam. The variable stiffness feature of extendable beams is widely observed in different applications (e.g., cranes [9], aerial ladders [10], and space structures [11]). Due to motion and external gust disturbance [12], [13], [14],

1083-4435 © 2024 IEEE. Personal use is permitted, but republication/redistribution requires IEEE permission.
See https://www.ieee.org/publications/rights/index.html for more information.

Authorized licensed use limited to: Hong Kong University of Science and Technology. Downloaded on August 28,2026 at 17:40:48 UTC from IEEE Xplore. Restrictions apply.

Fig. 2. (a) Scissor lift, (b) vertical mast lift, (c) articulating lift, (d) telescopic lift, and (e) telescopic articulating lift [8].

the long-beam extension generates variable-frequency structural vibrations, challenging for existing control techniques [14]. To investigate these vibration features, a telescopic lift is selected as the boom lift platform in this work.

The early investigations for structural vibration alleviation in boom lift structures exploit the feedforward methods. Moon [15] proposed to use the input shaping control method to suppress the boom lift vibrations. The method was further extended to the commandless input shaping technique (CIST) [16] to alleviate the vibration during unloading. Jia et al. [17] developed a two-mode zero-vibration input shaper to suppress the endpoint vibration considering multiple modes. To account for the model uncertainty and disturbances, Liu et al. [18] adopted a combination of feedforward CIST and feedback to suppress the vibrations. However, these existing methods are limited as they have not taken the parameter-varying vibration characteristics into consideration, which is key to BLMR [14].

Recent investigations have focused on vibration compensation with structure frequencies that change with different configurations. Yuan et al. [19] developed a time-varying input shaper (TVIS) to reduce the vibration of the boom lift system considering the extension beam. To enhance the robustness of the vibration compensation methods, feedback control is also introduced to alleviate the boom lift vibrations [13], [20], [21]. Nguyen et al. [20] proposed the PD controller via the feedback of rotational angle measurement of each segment to reduce the vibration based on the dynamic model established with modal parameters. Pertsch and Sawodny [10] established the infinite-dimensional model of the telescopic boom lift and utilized the observer-based state feedback controller with information from strain gauges and gyroscopes. Zimmert et al. [21] further combined the state feedback control based on the Euler–Bernoulli beam model with feedforward control to alleviate the vibration of the telescopic boom lift. However, these methods either require the modal parameters or only target a certain type of configuration.

Robotic-based vibration compensation methods are relatively mature but mostly address scenarios where the robots are mounted on a stationary foundation. Staufer and Gattringer [22] used the feedforward and classic feedback control combined with state estimation using angular rate and acceleration sensors to suppress the vibration. Shang et al. [23] proposed the neural network compensation sliding mode controller with a two-dimensional beam model to suppress the vibration of a two-inertia system with variable-length flexible load. Iterative learning input shaping with accelerator feedback [24] and adaptive finite impulse response input shaping using the strain gauge [25] are proposed to suppress the vibration. However, these robotic-based vibration compensation methods are limited in the BLMR scenarios since they either apply to the rotational joints or target repeatable works.

Recently the laser-tracker-based feedback control method [7] is proposed to alleviate the BLMR vibration, but the direct use of laser tracker measurement as feedback is expensive and prone to potential laser beam blocking during complex tasks. Therefore, a new feedback approach combining static deformation compensation and dynamic vibration compensation via IMU feedback is proposed to solve the extension-dependent vibration problem. Compared with existing solutions, the proposed method has a robot manipulator and IMU mounting on the tip of the general extendable beam structure and exploits robot manipulation for vibration compensation with no restrictions on joint types of extendable beam structures, no limitations on the type of robot manipulator on the tip (with enough redundancy), and no prior knowledge of modal parameters while automating the construction surface work. The core contributions are as follows.

1) A feedback vibration compensation method, Jacobian-based vibration compensation via IMU feedback (JVCI), is proposed to account for the extension-dependent vibration in general BLMR-type structures with a linear parameter varying system stability proof.
2) A representative telescopic BLMR capturing the extension-dependent vibration features is designed and built with an integrated electrical control system.
3) The proposed methods are verified in experiments with multidimensional analysis of vibration to show enhanced tracking accuracy and vibration alleviation, in contrast to the time-varying input shaping method [19].

The rest of this article is organized as follows. Section II describes the vibration compensation of BLMR, including the static deformation compensation, time-varying input shaping methods, and Jacobian-based vibration compensation via IMU feedback with stability proof. Section III discusses the BLMR design and experimental case studies to evaluate the proposed methods. Finally, Section IV concludes this article.

II. Vibration Compensation of BLMR

A. Kinematics of Telescopic BLMR

Considering a general BLMR configuration combining n_a electrical/pneumatic cylinders with a robotic manipulator with n_r joints, the boom lift actuator extension is defined as

$$d = \{d_1, d_2, \cdots, d_{n_a}\}^\top. \tag{1}$$

The robot joints are defined as

$$q = \{q_1, q_2, \cdots, q_{n_r}\}^\top \tag{2}$$

and the overall BLMR states are defined as

$$h = \left\{d^\top, q^\top\right\}^\top. \tag{3}$$

Define the inertial frame $\mathcal{F}_I$ attached to the ground, the body-fixed frame $\mathcal{F}_T$ attached to the tip, and the body-fixed frame $\mathcal{F}_E$

Authorized licensed use limited to: Hong Kong University of Science and Technology. Downloaded on August 28,2026 at 17:40:48 UTC from IEEE Xplore. Restrictions apply.

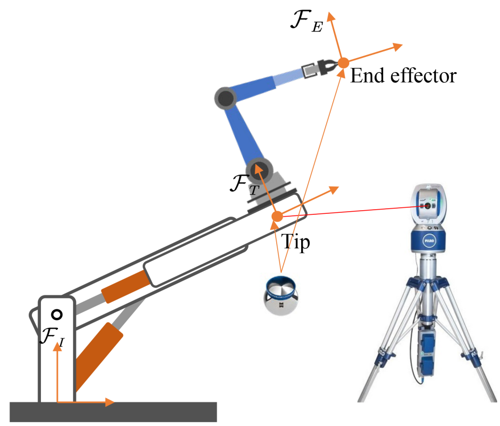

Fig. 3. Schematics of the BLMR with laser tracker measuring tip deflection.

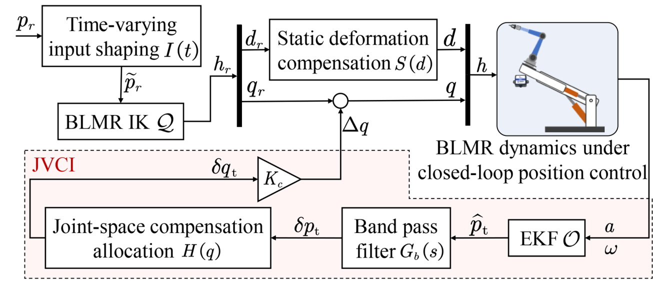

Fig. 4. Vibration compensation of the BLMR with feedforward and feedback methods.

attached to the end effector of the robotic manipulator, as shown in Fig. 3. Define the boom-lift-robot connection point $p_\mathrm{t}(d)$, and the robot's end effector position $p_\mathrm{e}(d,q)$, and the rotation Euler angle of the end effector (following ZYX rotation) is given by $\vartheta_\mathrm{e} \in \mathbb{R}^3$. The BLMR state velocity connects to the end effector velocity and angular velocity with the Jacobian matrix J, i.e.,

$$\begin{Bmatrix} \dot{p}_\mathrm{e} \\ \dot{\vartheta}_\mathrm{e} \end{Bmatrix} = \underbrace{\begin{bmatrix} & & \frac{\partial p_\mathrm{e}}{\partial h} & \\ {}^0_1Rz & {}^0_2Rz & \cdots & {}^{\ 0}_{n_r+n_a}Rz \end{bmatrix}}_{\triangleq J} \dot{h} \tag{4}$$

where z is the unit vector $\{0 \quad 0 \quad 1\}^\top$ along the local Z-direction for rotational joints and the zero vector $\{0 \quad 0 \quad 0\}^\top$ for prismatic joints, and ${}^0_iR$ is the rotation matrix from the frame corresponding to the ith actuator to the ground frame $\mathcal{F}_I$. The forward kinematics is given by (4). Note that the BLMR state is typically larger than six due to their combination of the boom lift and the robot degrees of freedom. Therefore, the corresponding inverse kinematics is redundant and cannot be uniquely defined. The inverse kinematics $\mathcal{Q}$ is a standard quadratic programming problem with linear constraints, given by

$$\delta h = W^{-1} J^\top \left(JW^{-1}J^\top\right)^{-1} \left\{\delta p_\mathrm{e}^\top, \delta\vartheta_\mathrm{e}^\top\right\}^\top \tag{5}$$

where δh, δp_e, and $\delta\vartheta_\mathrm{e}$ are the local perturbations around the states, and W is the positive definite weight matrix. Apart from the Jacobian of the robot end effector, the Jacobian of the boom lift tip point is also crucial as it accounts for the significant deviations due to the long beam deflections. To account for the nonlinear static deformation, the static error at the tip is measured with a laser tracker, as shown in Fig. 3, and is defined as $\bar{e}_\mathrm{t}(d)$. Exploiting the low-frequency nature of the deformation, the static deformation map generates the compensated boom lift actuator input δd, given by

$$\delta d = J_\mathrm{t}^\dagger \bar{e}_\mathrm{t}, \; J_\mathrm{t} = \frac{\partial p_\mathrm{t}}{\partial d} \tag{6}$$

where $J_\mathrm{t}^\dagger$ is the right pseudoinverse of J_t. The static deformation compensation $S(d)$ is given by

$$d = d_r + \delta d \tag{7}$$

where d_r is the desired boom lift actuator extension.

B. Jacobian-Based Vibration Compensation Via IMU Feedback

The motion of the BLMR introduces vibrations to the end effector due to the flexibility of the boom lift. The entire compensation scheme embracing different controllers is shown in Fig. 4. Static deformation is compensated with the deformation map to enhance the trajectory accuracy. The vibration is accounted for using Jacobian-based vibration compensation via IMU feedback (red region in Fig. 4), TVIS feedforward, and their reconfigurable combination.

Among the feedforward vibration suppression methods targeted for extension-dependent vibration characteristics, the TVIS method [19] is an effective method to alleviate the extension-dependent vibration. Assume the natural frequency $\omega_n(d)$ and the damping ratio $\xi(d)$ of the BLMR are known as a nonlinear function of the beam extension. In the implementation of TVIS, the natural frequency and damping ratio are scheduled with time, and this time-varying input shaping filter $I(t)$ is

$$I(t) = \frac{1}{1+L(t)} u(t) + \frac{L(t)}{1+L(t)} u\left(t - T_\mathrm{I}(t)\right) \tag{8}$$

where $u(t)$ is the impulse signal, $T_\mathrm{I}(t)$ and $L(t)$ are the time-varying time shift and ratio between impulses given by

$$\begin{aligned} T_\mathrm{I}(t) &= \frac{\pi}{\omega_n(t)\sqrt{1-\xi(t)^2}} \\ L(t) &= e^{\left(\frac{-\xi(t)\pi}{\sqrt{1-\xi(t)^2}}\right)}. \end{aligned} \tag{9}$$

The reference trajectory of the end effector $p_r(t)$ is convolved with $I(t)$ to get the modified reference $\tilde{p}_r(t)$ as

$$\tilde{p}_r(t) = \frac{1}{1+L(t)} p_r(t) + \frac{L(t)}{1+L(t)} p_r\left(t - T_\mathrm{I}(t)\right). \tag{10}$$

The reference trajectory $p_r(t)$ is assumed to have a sufficient constant ending portion to avoid steady-state error.

To suppress the vibration problems in real-time without prior knowledge of the natural frequency and damping ratio of BLMR, Jacobian-based vibration compensation via IMU feedback is proposed. To compensate for these vibrations, it is assumed that an IMU is attached to the bottom of the boom lift tip (as shown in Fig. 4). This arrangement arises from the fact that the extendable

Authorized licensed use limited to: Hong Kong University of Science and Technology. Downloaded on August 28,2026 at 17:40:48 UTC from IEEE Xplore. Restrictions apply.

long boom lift arms contribute to the major structural flexibility that needs to be accurately captured. The robotic manipulator is significantly stiffer and assumed to be following rigid-body motion. The overall BLMR states $h = \{d^\top, q^\top\}^\top$ are executed by the position controller of the actuator with a P-PI structure. The vibration at the tip is expected to be compensated for with the robotic manipulator, given by

$$q = q_r + \Delta q \tag{11}$$

where q_r is the desired robot joint input and Δq is the incremental joint movement to compensate for the vibration. Therefore, the joints' dynamic contribution needs to be established. We assume that the vibration structural modes depend on the boom lift actuator extension state d, and thus, model the dynamic system as a linear parameter varying system defined as $G_o(s; d)$, where s is the Laplace variable while the multidimensional d is a slowly varying parameter deciding the local vibration characteristics. The input and output of the system are the joint movement $q_i(t)$, and the acceleration $a(t)$ and angular velocity $\omega(t)$ from IMU measurement, respectively, such that

$$\left\{A_t^\top(s), \Omega_t^\top(s)\right\} = G_o(s; d)\, Q(s) \tag{12}$$

where $Q(s)$, $A_t(s)$, and $\Omega_t(s)$ are the Laplace transform of $q_i(t)$, $a(t)$, and $\omega(t)$, respectively.

The vibration of the tip is reconstructed via IMU measurement with an extended Kalman filter (EKF). The body-fixed frame $\mathcal{F}_T$ is related to the inertial frame $\mathcal{F}_I$ by a ZYX Euler angle rotation (defined as $\vartheta_\mathrm{t} \in \mathbb{R}^3$, $\vartheta_\mathrm{t} = \{\phi \quad \theta \quad \psi\}^\top$). The velocity of the tip is given by $v \in \mathbb{R}^3$. The dynamic model of IMU is defined as

$$\begin{aligned}\dot{\vartheta}_\mathrm{t} &= C(\vartheta_\mathrm{t})\,\omega \\ \dot{v} &= a - \omega \times v - R(\vartheta_\mathrm{t})\, g\end{aligned} \tag{13}$$

where $C(\vartheta_\mathrm{t})$ is defined as

$$C(\vartheta_\mathrm{t}) = \begin{bmatrix} 1 & \frac{\mathrm{s}_\phi \mathrm{s}_\theta}{\mathrm{c}_\theta} & \frac{\mathrm{c}_\phi \mathrm{s}_\theta}{\mathrm{c}_\theta} \\ 0 & \mathrm{c}_\phi & -\mathrm{s}_\phi \\ 0 & \frac{\mathrm{s}_\phi}{\mathrm{c}_\theta} & \frac{\mathrm{c}_\phi}{\mathrm{c}_\theta} \end{bmatrix} \tag{14}$$

and $R(\vartheta_\mathrm{t})$ is defined as

$$R(\vartheta_\mathrm{t}) = \begin{bmatrix} \mathrm{c}_\theta \mathrm{c}_\psi & \mathrm{c}_\theta \mathrm{s}_\psi & -\mathrm{s}_\theta \\ \mathrm{s}_\phi \mathrm{s}_\theta \mathrm{c}_\psi - \mathrm{c}_\phi \mathrm{s}_\psi & \mathrm{s}_\phi \mathrm{s}_\theta \mathrm{s}_\psi + \mathrm{c}_\phi \mathrm{c}_\psi & \mathrm{s}_\phi \mathrm{c}_\theta \\ \mathrm{c}_\phi \mathrm{s}_\theta \mathrm{c}_\psi + \mathrm{s}_\phi \mathrm{s}_\psi & \mathrm{c}_\phi \mathrm{s}_\theta \mathrm{s}_\psi - \mathrm{s}_\phi \mathrm{c}_\psi & \mathrm{c}_\phi \mathrm{c}_\theta \end{bmatrix} \tag{15}$$

where $\mathrm{s}_\kappa = \sin(\kappa)$ and $\mathrm{c}_\kappa = \cos(\kappa)$ ($\kappa = \phi, \theta, \psi$). Given the IMU model (13) to predict $\hat{\vartheta}_\mathrm{t}$, $\hat{v}$, and $\dot{\hat{p}}_\mathrm{t}$, the EKF $\mathcal{O}$ are defined as

$$\begin{Bmatrix} \dot{\hat{\vartheta}}_\mathrm{t} \\ \dot{\hat{v}} \\ \dot{\hat{p}}_\mathrm{t} \end{Bmatrix} = \begin{Bmatrix} C\left(\hat{\vartheta}_\mathrm{t}\right)\omega \\ a - \omega \times \hat{v} - R\left(\hat{\vartheta}_\mathrm{t}\right) g \\ \hat{v} \end{Bmatrix} + L\left(\hat{\vartheta}_\mathrm{t} - \vartheta_\mathrm{t}\right) \tag{16}$$

where L is the observer matrix. With estimated $\hat{p}_\mathrm{t}$, the tip vibration δp_t in the body-fixed frame $\mathcal{F}_T$ after the band pass filter system $G_b(s)$ is defined as

$$\delta p_\mathrm{t} = R_T\left(\hat{\vartheta}_\mathrm{t}\right)^\top \mathcal{L}^{-1}\left[G_b(s)\left(\hat{P}_\mathrm{t}(s) - P_\mathrm{t}(s)\right)\right] \tag{17}$$

where $R_T(\vartheta)$ is the rotation matrix from the inertial frame $\mathcal{F}_I$ to the body-fixed frame $\mathcal{F}_T$, $G_b(s)$ is utilized to eliminate the drift, and $\hat{P}_\mathrm{t}(s)$ and $P_\mathrm{t}(s)$ are the Laplace transform of the estimated tip position $\hat{p}_\mathrm{t}$ and the reference tip position p_t, respectively. The response of the industrial robot is assumed to be faster than that of the boom lift. High-frequency vibration can be compensated with a robot manipulator and the vibration of the end effector can be alleviated even if there exists a large vibration at the tip. Optimization-based allocation is proposed to reduce the vibration induced by each joint based on the criteria of minimum joint movement and change of mass center. The tip vibration δp_t is compensated via the incremental joint movement δq_t by solving the optimization problem $H(q)$, defined as

$$H = \min_{\delta q_\mathrm{t}} \left[w_1 \|\delta p_c\|_2 + w_2 \|\delta q_\mathrm{t}\|_2\right], \text{s.t.}\, \delta p_\mathrm{t} = J_r\, \delta q_\mathrm{t} \tag{18}$$

where w_1 and w_2 are the weights, J_r is the Jacobian matrix of the robot manipulator, and δp_c is the change of the robot center of mass defined as

$$\delta p_c = \frac{\partial f_m}{\partial q}\, \delta q_\mathrm{t} \tag{19}$$

where $f_m(\cdot)$ calculates the mass center of the robot manipulator. With this optimization problem solved, the incremental joint movement is given by

$$\Delta q = K_c\, \delta q_\mathrm{t} \tag{20}$$

where K_c is the feedback gain. The allocation of the increment movement of δp_t to each joint affects the vibration performance since the joints' dynamic contribution differs from each other. Optimization-based allocation via (18) is proposed to reduce the vibration induced by each joint.

The feedback stability of the JVCI method significantly depends on the design of K_c. The EKF and robot joint-space compensation allocation can be linearized as $G_e(s; d)$ and $G_a(d)$. The vibration at the tip is typically significantly faster than its nominal motion (planned trajectory with only d). Therefore, the stability of the system is analyzed from a conventional linear-parameter-varying (LPV) system framework with d as the scheduling parameter. Define the overall open-loop system as

$$G(s; d) = K_c\, G_a(d)\, G_b(s)\, G_e(s; d)\, G_o(s; d). \tag{21}$$

The stability of the system is guaranteed by the generalized Nyquist theorem for the multiple-input multiple-output (MIMO) system, where $G(j\omega_f; d)$ is experimentally measured. Let P_{ol} denote the number of open-loop unstable poles in the open-loop MIMO transfer function matrix $G(s; d)$. The closed-loop system is stable if and only if the Nyquist plot of $\det(I + G(s; d))$ makes P_{ol} anticlockwise encirclements of the origin and does not pass through the origin [26]. For the typically open-loop stable BLMR system, this theorem demands no origin encirclements of the $\det(I + G(s; d))$.

Authorized licensed use limited to: Hong Kong University of Science and Technology. Downloaded on August 28,2026 at 17:40:48 UTC from IEEE Xplore. Restrictions apply.

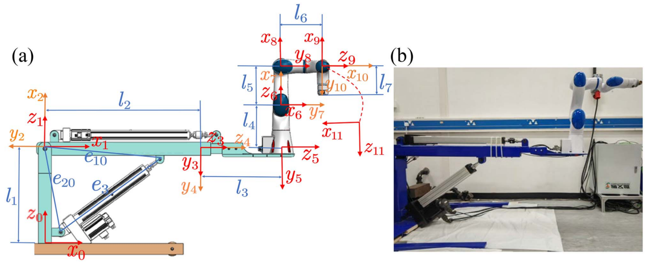

Fig. 5. (a) BLMR schematics with the definitions of DH reference frames and (b) the BLMR prototype.

TABLE I
SPECIFICATIONS OF THE BLMR PROTOTYPE

Load (kg)				3			
Vertical range (m)				0.4–3.5			
Motion range of d (m) and q (°)							
d_1		d_2		q_1		q_2	
0–0.4		0–0.7		-180–180		-120–120	
q_3		q_4		q_5		q_6	
-140–140		-180–180		-130–130		-180–180	
Maximum speeds of $\dot{d}_m$ (m/s) and $\dot{q}_m$ (°/s)							
$\dot{d}_{1m}$	$\dot{d}_{2m}$	$\dot{q}_{1m}$	$\dot{q}_{2m}$	$\dot{q}_{3m}$	$\dot{q}_{4m}$	$\dot{q}_{5m}$	$\dot{q}_{6m}$
0.15	0.25	120	90	90	240	240	240

III. EXPERIMENTS ON A BLMR PROTOTYPE

A. Prototype Design and Hardware Setup

To verify the proposed methods, a scaled BLMR prototype is designed and built by combining a telescopic boom lift and a Huashu HSR-Co603 collaborative robot, as shown in Fig. 5(b). The boom lift's two joints are actuated by two electromechanical cylinders (EMCs) driven by Panasonic MSMF302L1H6M and MSMF082L1V2M servo motors. A Jobrey Tech IMU, with an acceleration resolution of 0.0002 g and angular speed resolution of 0.01 °/s, is attached to the tip of the boom lift for real-time feedback. The robot joints, EMCs, and IMU are all controlled and sensed in real-time with the Beckhoff TwinCAT system via EtherCAT and RS485 communications with a 1 kHz sampling rate. The vibration or deformation is measured by FARO Vantage^{E6} Max laser tracker with a distance resolution of 50 μm, as shown in Fig. 3. The detailed specifications of the BLMR prototype are listed in Table I.

B. Kinematic Modeling

The schematics of the BLMR are shown in Fig. 5(a) and the blue triangle illustrates the initial configuration of BLMR. The length of each side of the blue triangle at the initial configuration is e_{10}, e_{20}, and e_{30}. For ease of calculation, the movement of d_1 is converted to the rotation of the link q_{d1} as

$$\begin{aligned} q_{d1} &= \cos^{-1}\left(\left({e_{10}}^2 + {e_{20}}^2 - {e_3}^2\right)/2e_{10}e_{20}\right) - \alpha \\ \alpha &= \cos^{-1}\left(\left({e_{10}}^2 + {e_{20}}^2 - {e_{30}}^2\right)/2e_{10}e_{20}\right) \\ e_3 &= e_{30} + d_1. \end{aligned} \tag{22}$$

TABLE II
DENAVIT–HARTENBERG TABLE OF THE BLMR

i	α_{i-1}	a_{i-1}	d_i	θ_i
1	0	0	l_1	0
2	$\pi/2$	0	0	$\pi/2 + q_{d1}$
3	$\pi/2$	0	l_2	$\pi/2$
4	0	0	d_2	0
5	0	0	l_3	0
6	$\pi/2$	0	l_4	$\pi/2 + q_1$
7	$-\pi/2$	0	0	$q_2 - \pi/2$
8	0	l_5	0	q_3
9	$-\pi/2$	0	l_6	q_4
10	$\pi/2$	0	0	$\pi/2 + q_5$
11	$-\pi/2$	0	0	$\pi + q_6$

In the given motion ranges, d_1 and q_{d1} formulate a bijection and d_1 can be recovered from q_{d1} with

$$d_1 = \sqrt{{e_{10}}^2 + {e_{20}}^2 - 2\cos\left(q_{d1} + \alpha\right) e_{10}e_{20}} - e_{30}. \tag{23}$$

The variable set can be rewritten as

$$\tilde{h} = \left\{q_{d1} \quad d_2 \quad q_1 \quad q_2 \quad q_3 \quad q_4 \quad q_5 \quad q_6\right\}^{\top}. \tag{24}$$

The detailed Denavit–Hartenberg (DH) frames of the BLMR are illustrated in Fig. 5(a), and the DH table is shown in Table II. The overall transformation matrix from the ground to the end effector frame is given by

$$T = T_1 \, T_2 T_3 T_4 T_5 T_6 T_7 T_8 T_9 T_{10} T_{11}. \tag{25}$$

The position of the end effector is

$$p_{\mathrm{e}} = Tl \tag{26}$$

where l is the tool in the end effector frame. J is given by

$$J = \begin{bmatrix} & & & & \frac{\partial p_{\mathrm{e}}}{\partial \tilde{h}} & & & \\ {}^0_2Rz_1 & z_0 & {}^0_6Rz_1 & {}^0_7Rz_1 & {}^0_8Rz_1 & {}^0_9Rz_1 & {}^0_{10}Rz_1 & {}^0_{11}Rz_1 \end{bmatrix} \tag{27}$$

where $z_1 = \{0 \quad 0 \quad 1\}^{\top}$ is for the rotational joints, and $z_0 = \{0 \quad 0 \quad 0\}^{\top}$ is for the prismatic joints.

To enhance end effector positioning, static deformation compensation is first exploited. With the robot standing on the tip, the EMC extension d_1 and d_2 are sampled with a 50 mm spacing to formulate a sampling grid, where d_1 starts from 0 to 400 mm and d_2 is from 0 to 700 mm. With the laser tracker measurement, the static deformation map of the boom lift tip is generated automatically via designed software, as presented in Fig. 6. Note that this deformation is typically a smooth nonlinear function. Therefore, even for high-dimensional deformation maps of full-scale boom lifts with more degrees of freedom and uncertain payload, adaptive meshing techniques and surrogate models [27] could be exploited to reduce the number of required samples. The deformation $\bar{e}_{\mathrm{t}}$ of the X-direction, Z-direction, and their total deformation are plotted in both work and joint spaces. They are defined as $\mathcal{M}_{Cx}$, $\mathcal{M}_{Cz}$, $\mathcal{M}_{Ct}$, $\mathcal{M}_{Jx}$, $\mathcal{M}_{Jz}$, and $\mathcal{M}_{Jt}$, respectively. The deformation is mainly caused by the moment relative to the base arising from the payload gravity. The

Authorized licensed use limited to: Hong Kong University of Science and Technology. Downloaded on August 28,2026 at 17:40:48 UTC from IEEE Xplore. Restrictions apply.

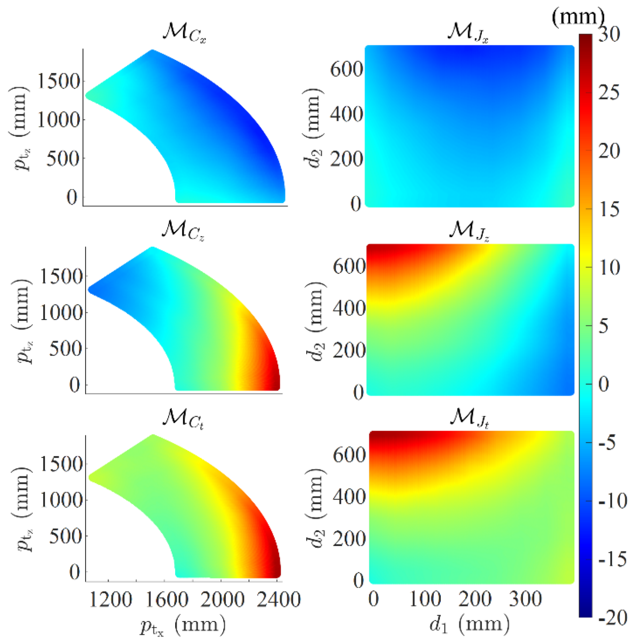

Fig. 6. Static deformation map in the work and joint space.

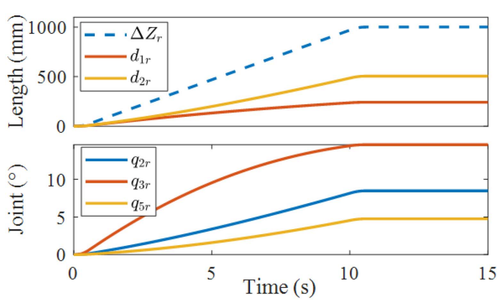

Fig. 7. Reference trajectory of the end effector and IK result.

deformation map in the workspace shows that the deformation mainly lies in the Z-direction and grows as the boom lift extends further. The deformation map in the joint space shows that the extension d_2 impacts the deformation more as the beam extension leads to a larger moment.

To verify the static deformation compensation, the BLMR is commanded to follow a velocity and acceleration constrained 1-m elevation trajectory (dashed line in Fig. 7) with the initial condition given by

$$p_{e0} = \left\{2209.5058 \quad 0 \quad 1300.4401 \quad 0 \quad \tfrac{\pi}{2} \quad 0\right\}^{\top}. \tag{28}$$

The corresponding initial joint position $\tilde{h}_0$ is

$$\tilde{h}_0 = \left\{0 \quad 0 \quad 0 \quad 0 \quad 0 \quad 0 \quad -\tfrac{\pi}{2} \quad 0\right\}^{\top}. \tag{29}$$

The corresponding EMC trajectory d and robot trajectory are calculated with (5) and are plotted in Fig. 7. It is assumed that the d_{1r} and d_{2r} are the reference movement of two EMCs and q_{2r}, q_{3r}, and q_{5r} are the reference movement of the robot joints while the rest of joints q_{1r}, q_{4r}, and q_{6r} remain zero. The end effector tracking error e_x and e_z in the X- and Z-directions with

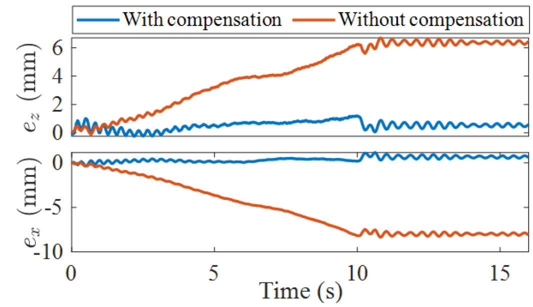

Fig. 8. Open-loop BLMR end effector tracking error with and without static deformation compensation.

TABLE III
SSE AND RMSE OF TRAJECTORY WITH AND WITHOUT STATIC DEFORMATION COMPENSATION

	SSE (mm)	RMSE (mm)
With Compensation	0.8602	0.7197
Without Compensation	10.2252	6.0562

and without the static deformation compensation are captured with a laser tracker and illustrated in Fig. 8. The deviation of uncompensated trajectory from the reference grows as the EMCs extends. The steady-state error (SSE) and root-mean-square error (RMSE) of the trajectory with and without compensation are shown in Table III. The motion accuracy is enhanced by the static deformation compensation while oscillation exists due to the flexibility of the BLMR. The current static deformation compensation scheme has limitations and does not eliminate the SSE. The deformation at each point is estimated using cubic interpolation with the static deformation map. The static deformation map is constructed with the robot fixed on the BMLR tip while the different configurations of the industrial robot also affect the boom lift deformation.

C. Vibration Compensation of the BLMR Prototype

Similar tracking experiments are exploited to evaluate the feedforward trajectory generation method TVIS [19], the proposed feedback control method JVCI, as well as their combinations to alleviate the motion-induced vibration of the BLMR. TVIS requires the natural frequency and damping ratio of BLMR to be continuously updated. Natural frequency and damping ratio maps of the BLMR system are captured with a laser tracker capturing the impact responses, similar to the deformation map sampling grid. For BLMR and general extendable beam systems, the first bending mode is dominant. The damping ratio is calculated with the first few resonant peaks and troughs [28] under the first bending mode, given by

$$\xi(d) = \frac{\ln\left(\frac{\sum Y_{2k-1}}{\sum Y_{2k}}\right)}{\sqrt{(\pi)^2 + \left(\ln\left(\frac{\sum Y_{2k-1}}{\sum Y_{2k}}\right)\right)^2}} \tag{30}$$

where Y_{2k-1} and Y_{2k} are the peak and trough in the oscillatory impact responses. It is observed that the damping ratio

Authorized licensed use limited to: Hong Kong University of Science and Technology. Downloaded on August 28,2026 at 17:40:48 UTC from IEEE Xplore. Restrictions apply.

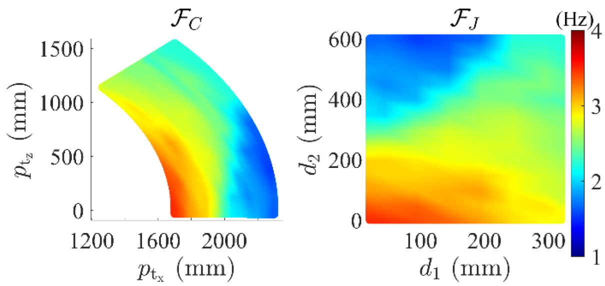

Fig. 9. Natural frequency map of BLMR under different extension states.

difference with different extensions is small. As the number of sets of peaks and troughs used to calculate the damping ratio increases, an average value converges to 0.0387 and is applied across the extension space. With this damping ratio, the natural frequency map is calculated from the resonances in the impact responses. Frequency maps in the workspace and joint space are defined with $\mathcal{F}_C$ and $\mathcal{F}_J$, respectively, as shown in Fig. 9. In contrast to the uniform damping ratio, the natural frequency map exhibits the variation, especially along d_2 direction. The natural frequency decreases as the BLMR reaches a further or higher position. The parameters of TVIS are estimated using cubic interpolation via the frequency map.

The feedback control method JVCI regulates the vibrations in the XZ plane, and thus, three joints q_2, q_3, and q_5 are exploited to compensate for the vibration of p_{t}. According to IMU acceleration and angular speed resolution, the covariance matrices of state function and measurement in the EKF are set to diag$\{0.01, 0.01, 0.01, 0.001, 0.001, 0.001, 0.1, 0.1, 0.1\}$ and diag$\{0.01, 0.01, 0.01\}$. The Jacobian constraint $\delta p_{\mathrm{t}} = J_r \ \delta q_{\mathrm{t}}$ in (18) is underdetermined, leaving room for optimization. The underdetermined constraints are exploited to reduce the optimization variables to only $\delta q_{\mathrm{t}5}$ to convert the problem into an unconstrained optimization. This reduces the computational load and enables the real-time solution of the optimization problem (18). To account for their different nominal values, the coefficients w_1 and w_2 are set to 1 and 5×10^6. The vibration δp_{t} is allocated to the industrial robot following (18).

Since the change of the extension lengths is sufficiently slow compared to the structural dynamics, the stability of the LPV system is guaranteed if the JVCI feedback control is stable at all extension lengths [29]. The BLMR open-loop system $G_o(s; d)$ from the robotic joints q_2, q_3, and q_5 to the tip vibration is identified at different extension states, and d_1 and d_2 are sampled with 125 and 250 mm spacing, respectively. The mth d_1 sample and the nth d_2 sample are defined as d_{mn}, formulating a sampling grid. The sinusoidal references with different frequencies and amplitudes are commanded to q_2, q_3, and q_5 to measure the corresponding responses of $a(t)$ and $\omega(t)$. This sequence also formulates a set of frequency response functions (FRFs) $G_o(j\omega_f; d_{mn})$, where ω_f is the measured frequency. Each measured FRF corresponds to a point in the sampling grid of d; this FRF builds the overall open-loop LPV transfer function following (21). The stability of this LPV system is verified with the closed-loop stability of the generalized Nyquist theorem [26]. The Nyquist plot $\mathcal{C}_{mn}$ of the closed-loop system with different gains under different extension states is shown in Fig. 10. The sampling interval of gain K_c is set as 10 for better visualization. To ensure the stability of the system, the red dot at the origin should be outside the encirclements. According to this rule, the gain K_c is set to 40 in the experiment.

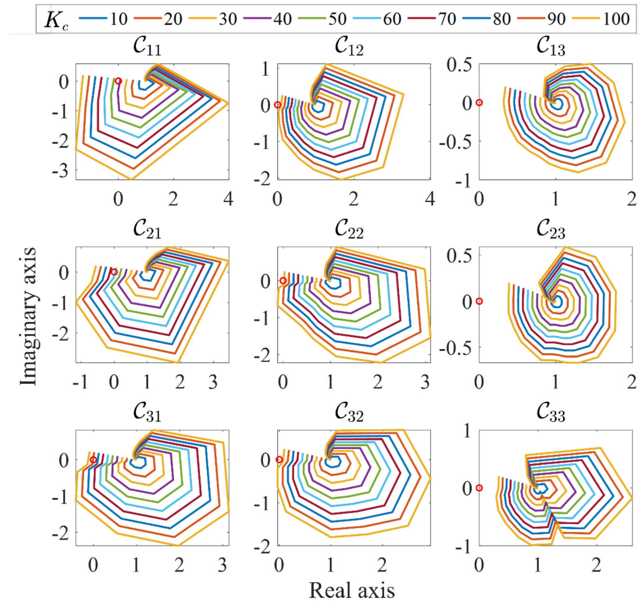

Fig. 10. Nyquist diagram $\mathcal{C}_{mn}$ of the closed-loop system $G_c(s)$ with different extension length d_{mn}.

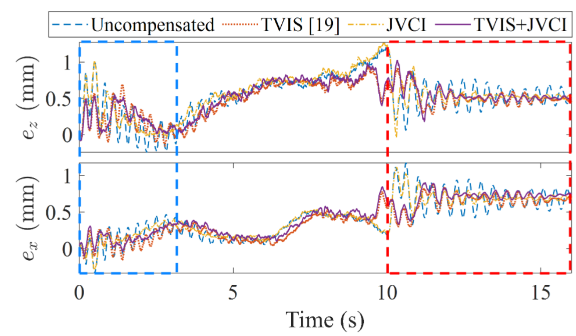

Fig. 11. End effector tracking error of the BLMR without compensation, with TVIS [19], JVCI, and their combination.

With settled parameters, the TVIS [19], JVCI, and their combination are implemented on the BLMR. The tracking error e_x and e_z in the X- and Z-directions are presented in Fig. 11. To evaluate the performance, in addition to the peak value of the fast Fourier transform of the vibration signal at the beginning (0–3 s, blue dotted box) and the end (10–16 s, red dotted box), as shown in Fig. 12, the convergence time of residual vibration is also considered, defined as the time when the amplitude of the vibration is less than 0.05 mm after the BMLR stops motion. The average vibration reduction percentage R is defined as

$$R = 1 - \frac{1}{2}\left(\frac{A_{c1}}{A_{u1}} + \frac{A_{c2}}{A_{u2}}\right) \tag{31}$$

Authorized licensed use limited to: Hong Kong University of Science and Technology. Downloaded on August 28,2026 at 17:40:48 UTC from IEEE Xplore. Restrictions apply.

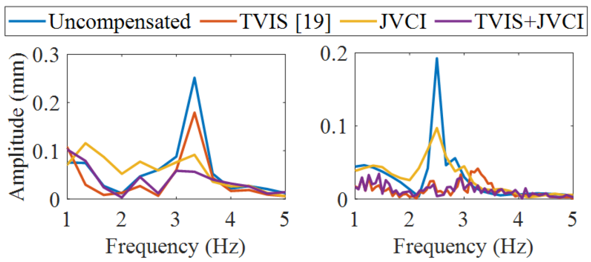

Fig. 12. Spectrum of the tracking error of the BLMR with no compensation, TVIS [19], JVCI, and their combination at the beginning (left) and the end (right).

TABLE IV
TRACKING PERFORMANCE WITH NO COMPENSATION, TVIS [19], JVCI, AND THEIR COMBINATION

Methods	Peak value at beginning/ end (mm)	Convergence time (s)	Average vibration reduction percentage
No compensation	0.2515/ 0.1925	> 6	/
TVIS [19]	0.1791/ 0.0416	≈ 4	53.59%
JVCI	0.0916/ 0.0971	≈ 3.5	56.57%
Combination	0.0584/ 0.0291	≈ 3	80.83%

where A_{c1} and A_{c2} are the compensated peak values at the beginning and the end; A_{u1} and A_{u2} are the uncompensated peak values at the beginning and the end, and the peak values are shown in Fig. 12. The detailed comparison is shown in Table IV. It is observed that all the vibration compensation methods reduced vibration. The performance of JVCI is enhanced compared with TVIS as it considers the disturbances from robot movement in real-time. TVIS highly depends on the accuracy of the natural frequency and damping ratio map, but constructing such maps with smaller grids takes more cost. TVIS is designed to compensate for vibration induced during movement trajectories and is not effective in static scenes where there is no movement. The combination of JVCI and TVIS further improves the tracking performance, indicating that the combination is a promising approach for vibration alleviation in boom lifts. This shows the potential to combine the JVCI with TVIS via rough natural frequency and damping ratio map to achieve enhanced performance with less cost.

IV. Conclusion

To automate construction surface work, this work investigates the vibration compensation of a BLMR system. The characteristic extension-dependent static and vibration dynamics of BLMR are addressed with systematic combinations of static deformation compensation and Jacobian-based vibration compensation via inertial measurement unit feedback. To verify the methods, a BLMR prototype is designed and built, with its extension-dependent static error and vibration characteristics experimentally identified. The performances of the proposed vibration compensation methods are compared to a time-varying input shaping method to illustrate enhanced tracking performance under motion-induced BLMR vibration.

References

[1] K. H. Petersen, N. Napp, R. Stuart-Smith, D. Rus, and M. Kovac, “A review of collective robotic construction,” *Sci. Robot.*, vol. 4, no. 28, pp. 1–28, 2019.

[2] N. Melenbrink, J. Werfel, and A. Menges, “On-site autonomous construction robots: Towards unsupervised building,” *Automat. Construction*, vol. 119, no. 5, 2020, Art. no. 103312.

[3] D. K. Liu et al., “A robotic system for steel bridge maintenance: Research challenges and system design,” in *Proc. Australas. Conf. Robot. Automat.*, 2008, pp. 1–7.

[4] H. Dai, “Design of high-altitude curtain wall cleaning robot,” in *Proc. 3rd World Conf. Mech. Eng. Intell. Manuf.*, 2020, pp. 157–160.

[5] J. W. Cho, J. H. Lee, Y. S. Kim, and K. C. Shin, “An analysis model for wind resistance performance of automated exterior wall painting robots in apartment buildings,” *KSCE J. Civil Eng.*, vol. 18, no. 4, pp. 909–919, 2014.

[6] L. Yang et al., “Automated wall-climbing robot for concrete construction inspection,” *J. Field Robot.*, vol. 40, no. 1, pp. 110–129, 2023.

[7] S. J. Keating, J. C. Leland, L. Cai, and N. Oxman, “Toward site-specific and self-sufficient robotic fabrication on architectural scales,” *Sci. Robot.*, vol. 2, no. 5, 2017, Art. no. 26595.

[8] Genie, “Genie,” *Terex Corporation*, 2023. [Online]. Available: https://www.genielift.com/en

[9] M. Ambrosino, A. Dawans, and E. Garone, “Constraint control of a boom crane system,” in *Proc. 37th Int. Symp. Automat. Robot. Construction*, 2020, pp. 499–506.

[10] A. Pertsch and O. Sawodny, “Modelling and control of coupled bending and torsional vibrations of an articulated aerial ladder,” *Mechatronics*, vol. 33, pp. 34–48, 2016.

[11] M. Duan, C. E. S. Cesnik, I. V. Kolmanovsky, and F. Vetrano, “Control-oriented modeling for flexible aircraft,” *J. Aircr.*, vol. 61, no. 1, pp. 183–195, 2024.

[12] M. Duan, D. Yoon, and C. E. Okwudire, “A limited-preview filtered b-spline approach to tracking control – with application to vibration-induced error compensation of a 3D printer,” *Mechatronics*, vol. 56, pp. 287–296, 2018.

[13] C. H. Chou, M. Duan, and C. E. Okwudire, “A physics-guided data-driven feedforward tracking controller for systems with unmodeled dynamics – Applied to 3D printing,” *IEEE Access*, vol. 11, pp. 14563–14574, 2023.

[14] M. Deng, A. Ji, L. Zhang, H. Wang, and Z. Zhao, “Lateral vibration behaviors of the straight boom of the aerial work platform in the horizontal linear motion,” *Automat. Construction*, vol. 134, Dec. 2021, Art. no. 104095.

[15] K. S. Moon, “Input shaping control for suppression of boom vibrations,” in *Proc. IEEE Int. Conf. Automat. Sci. Eng.*, 2012, pp. 782–785.

[16] J. Y. Park and P. H. Chang, “Vibration control of a telescopic handler using time delay control and commandless input shaping technique,” *Control Eng. Pract.*, vol. 12, no. 6, pp. 769–780, 2004.

[17] H. Jia, F. Zhu, and V. Joshua, “Using input shaping to repress two-mode residual vibration on aerial lifts,” in *Proc. Int. Conf. Control, Automat. Syst.*, 2012, pp. 667–671.

[18] R. Liu, Y. Gao, S. Yang, and Y. Yang, “Vibration control of the boom system of truck-mounted concrete pump based on constant-position commandless input shaping technique,” *Shock Vib.*, vol. 2015, 2015, Art. no. 420935.

[19] Q. H. Yuan, J. Lew, and D. Piyabongkarn, “Motion control of an aerial work platform,” in *Proc. Proc. Amer. Control Conf.*, 2009, pp. 2873–2878.

[20] V. T. Nguyen, T. Schmidt, and T. Leonhardt, “A new active vibration control method on a ladder of turntable ladders,” *J. Mech. Sci. Technol.*, vol. 35, no. 6, pp. 2337–2345, 2021.

[21] N. Zimmert, A. Pertsch, and O. Sawodny, “2-DOF control of a fire-rescue turntable ladder,” *IEEE Trans. Control Syst. Technol.*, vol. 20, no. 2, pp. 438–452, Mar. 2012.

[22] P. Staufer and H. Gattringer, “State estimation on flexible robots using accelerometers and angular rate sensors,” *Mechatronics*, vol. 22, no. 8, pp. 1043–1049, 2012.

Authorized licensed use limited to: Hong Kong University of Science and Technology. Downloaded on August 28,2026 at 17:40:48 UTC from IEEE Xplore. Restrictions apply.

[23] D. Shang, X. Li, M. Yin, and F. Li, “Vibration suppression for two-inertia system with variable-length flexible load based on neural network compensation sliding mode controller and angle-independent method,” *IEEE/ASME Trans. Mechatronics*, vol. 28, no. 2, pp. 848–859, Apr. 2023.
[24] J. Park, P. H. Chang, H. S. Park, and E. Lee, “Design of learning input shaping technique for residual vibration suppression in an industrial robot,” *IEEE/ASME Trans. Mechatronics*, vol. 11, no. 1, pp. 55–65, Feb. 2006.
[25] M. O. T. Cole and T. Wongratanaphisan, “A direct method of adaptive fir input shaping for motion control with zero residual vibration,” *IEEE/ASME Trans. Mechatronics*, vol. 18, no. 1, pp. 316–327, Feb. 2013.
[26] S. Skogestad and I. Postlethwaite, *Multivariable Feedback Control: Analysis and Design*. New York, NY, USA: Wiley, 2005.
[27] Z. Zhai, H. Li, and X. Wang, “An adaptive sampling method for kriging surrogate model with multiple outputs,” *Eng. Comput.*, vol. 38, no. s1, pp. 277–295, 2022.
[28] F. L. Huang, X. M. Wang, Z. Q. Chen, X. H. He, and Y. Q. Ni, “A new approach to identification of structural damping ratios,” *J. Sound Vib.*, vol. 303, no. 1/2, pp. 144–153, 2007.
[29] J. Mohammadpour and C. W. Scherer, *Control of Linear Parameter Varying Systems With Applications*. New York, NY, USA: Springer, 2012.

Yi Zhou received the B.S. degree in aircraft design and engineering from Northwestern Polytechnical University, Xi’an, China, in 2020 and the M.S. degree in mechanical and automation engineering from The Chinese University of Hong Kong, Hong Kong, in 2022. He is currently working toward the Ph.D. degree in mechanical engineering with the Department of Mechanical and Aerospace Engineering, The Hong Kong University of Science and Technology, Hong Kong.

His research interests include robot modeling and control, and vibration control.

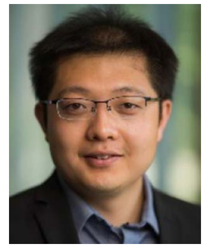

Molong Duan (Member, IEEE), received the B.S. degree in theoretical and applied mechanics from Peking University, Beijing, China, in 2012, and the M.S. and Ph.D. degrees in mechanical engineering from the Department of Mechanical Engineering, University of Michigan, Ann Arbor, MI, USA, in 2013 and 2018, respectively.

He is currently an Assistant Professor with the Department of Mechanical and Aerospace Engineering, The Hong Kong University of Science and Technology. His research interests include the modeling and control of advanced manufacturing systems, flexible structures, and robots.

Authorized licensed use limited to: Hong Kong University of Science and Technology. Downloaded on August 28,2026 at 17:40:48 UTC from IEEE Xplore. Restrictions apply.